Chemical Science

ROYAL SOCIETY OF CHEMISTRY

EDGE ARTICLE

View Article Online
View Journal | View Issue

Cite this: *Chem. Sci.*, 2025, **16**, 7811

All publication charges for this article have been paid for by the Royal Society of Chemistry

Fluorine-rich interface for garnet-based high-performance all-solid-state lithium batteries†

Shruti Suriyakumar, *[a] Indu M. Santhakumari, [a] Souvik Ghosh,[ab] Anju Vakakuzhiyil Gopinathan,[c] Sooraj Kunnikuruvan *[de] and Manikoth M. Shaijumon *[ab]

Solid-state batteries present a promising avenue that offers improved safety and energy density, effectively addressing the limitations of state-of-the-art lithium-ion batteries. Among different solid electrolytes, composite polymer electrolytes (CPEs) offer versatile multi-component solutions to distinct challenges posed by inorganic solid and organic polymer electrolytes. However, the polymer–filler interface issues significantly hamper their performance when higher ceramic (>20%) loading occurs. Here, we demonstrate an efficient strategy to introduce an *in situ*-formed fluorine-rich interface for the lithium anode and the ceramic fillers in the CPE. The rationally designed CPE comprises a high ceramic loading of 40% and exhibits significantly high Li-ionic conductivity (10^{-4} S cm^{-1} @ 55 °C) and compatibility, along with impressive long cycling performance of the Li|Li symmetric cell for over 2000 cycles at 0.1 mA cm^{-2}. We fabricated all-solid-state Li//LFP full cells that delivered a discharge capacity of 140 mA h g^{-1} at a 0.1C-rate when cycled at 70 °C and showed good cycling stability. The role of fluorine-containing additives in enhancing conductivity was validated using computations. Furthermore, we extended the applicability of the optimised CPE as an interface modifier in Li//LFP full cells, resulting in improved capacity and long-term cycling.

Received 12th February 2025
Accepted 26th March 2025

DOI: 10.1039/d5sc01107h

rsc.li/chemical-science

Introduction

The global transition from gasoline to electric vehicles (EVs) is currently underway,[1–3] and there is an urgent need for innovative material design and development leading to performance breakthroughs in battery technology in terms of rapid charging and high energy density.[4,5] Although lithium-ion battery-powered technology is flourishing, there is a need for increased safety and improved performance. Therefore, the scope and need for further scientific advancements are extensive.[6,7] There are dangers associated with the liquid electrolyte in a conventional battery pack due to its flammability, and this also limits us from exploring high-voltage cathodes and a metallic lithium anode. Also, graphite is unsuitable for rapid charging due to its sluggish reaction kinetics and risk of lithium plating.[8–10]

Replacing liquid electrolytes with non-flammable superionic conductive solid electrolytes, and graphite with metallic lithium will assist in overcoming the above limitations.[11–14] However, the challenges associated with using solid electrolytes with lithium, particularly interface issues and poor room-temperature conductivity, have to be addressed.[15–18] The two broad categories of solid electrolytes include inorganic solid pellets and composite polymer-based membranes. The biggest challenge with using rapid lithium-conducting conventional garnet and NASICON-based solid electrolytes is the need for high-temperature sintering to achieve optimum densification and additional interface engineering.[19–22] Conversely, polymer-based electrolytes, predominantly poly(ethylene oxide) (PEO) and Li salt-based electrolytes, are a viable option.[23,24]

Compared to other polymers, the complex formed between PEO and the salt imparts high ionic conductivity in the elastomeric phase at temperatures above the melting point of PEO and, hence, has been widely adopted.[25] Its drawbacks include poor strength and low tolerance to high current density. Although there have been many attempts to include passive fillers, such as Al_2O_3, SiO_2, and MOFs and active fillers, such as

[a]*School of Physics, Indian Institute of Science Education and Research Thiruvananthapuram, Vithura, Thiruvananthapuram, Kerala 695551, India. E-mail: shruti@iisertvm.ac.in; shaiju@iisertvm.ac.in*

[b]*Center for Advanced Materials Research with International Engagement (CAMRIE), Indian Institute of Science Education and Research Thiruvananthapuram, Maruthamala PO, Vithura, Kerala, 695551, India*

[c]*Department of Chemistry, SRM Institute of Science and Technology, Kattankulathur, Tamil Nadu 603203, India*

[d]*Department of Chemistry, Indian Institute of Technology Madras, Chennai 600036, India. E-mail: soorajk@iitm.ac.in*

[e]*Centre for Atomistic Modelling and Materials Design & Centre for Molecular Materials and Functions, Indian Institute of Technology Madras, Chennai 600036, India*

† Electronic supplementary information (ESI) available: Experimental details and computational studies of the sample (PDF), thermal stability test (MP4 Video file, VS1), demonstration of flexible battery (MP4 Video file, VS2). See DOI: https://doi.org/10.1039/d5sc01107h

oxides, NASICONS, argyrodites, and sulfides,[26,27] researchers tend to use batteries that operate at very low filler concentrations (<10%).

A promising solution is increasing research on composite electrolytes with high active filler loading to synergistically benefit from the design. However, the maximum limit of the filler concentration remains debated.[28–31] This is presumably due to the preferential change in the lithium-ion conduction pathway *via* the composite electrolyte. There are three possible ionic pathways: (1) through PEO–LiTFSI, (2) through PEO–LiTFSI and the active filler interface, or/and (3) through the filler. NMR studies by Hu *et al.* to probe the local structural Li environment reveal that Li-ion prefers the LLZO ceramic phase over polymer or its interface.[32]

Additionally, several findings demonstrate that the ceramic–polymer interface offers high resistance due to surface impurities and abrupt changes in the Li-ion concentration.[33] The concepts of space-charge region and phase distribution have been theoretically established to trace the percolation pathway and estimate the targeted design, such as filler loading and salt concentration.[34,35] It is well established that moving from ceramic-in-polymer- to polymer-in-ceramic- based electrolytes helps in dendrite suppression.[36]

There are non-uniform nucleation sites in lithium metal that cause the growth of lithium dendrites. The phenomenon is more prominent in liquid and polymer-based electrolytes. Many interface-directed works have been proposed, including using organic coatings and electrolyte additives, such as fluoroethylene carbonate (FEC), as well as artificial solid electrolyte interfaces (SEI), and metal coatings. For solid-state architectures, although numerous high-profile fluorine-based modifications are proposed (Scheme 1),[37–51] the homogeneous distribution of fluorine still remains a major challenge to be addressed.[52]

Herein, we demonstrate an efficient strategy to introduce an *in situ*-formed fluorine-rich interface for the lithium anode as well as the ceramic fillers in a composite polymer electrolyte (CPE). We show that a CPE prepared with a high ceramic loading of 40% along with a new fluorine-based additive, namely fluorostyrene, exhibits a significantly high Li-ionic conductivity (10^{-4} S cm^{-1} @ 55 °C) and compatibility, with an impressively long cycling performance of the Li|Li symmetric cell over 2000 cycles at 0.1 mA cm^{-2}. Control experiments and density functional theory (DFT) calculations were performed to decipher the role of fluorine incorporation, and the predictions based on binding energy calculations were found to agree with the experimentally observed trend in ionic conductivities. Furthermore, we extended the applicability of the optimised CPE as an interface modifier in Li//lithium iron phosphate (LFP) full cells, which was shown to stabilise the lithium metal anode and the LFP cathode, resulting in improved capacity and long-term cycling.

We highlight that the fluorostyrene additive exhibits superior properties, is less expensive, and is required in lesser quantity than the well-explored FEC[53,54] additive. Concerning the requirements of the EV sector, our findings underscore the importance of high ceramic loading and a stable interface to facilitate long-term cycling. Our approach not only eliminates the issues associated with high garnet loading but also offers an exceptionally stable interface for a long cycling range.

Results and discussion

We synthesized a ceramic filler, Al-doped $Li_{6.28}Al_{0.24}La_3Zr_2O_{12}$ (Al-LLZO), using a conventional solid-state reaction method, and subsequently characterized the filler as detailed in the ESI (Fig. S1).† The PEO : LiTFSI weight ratio was fixed at 5 : 1, and the ceramic-loaded composite electrolyte was prepared by

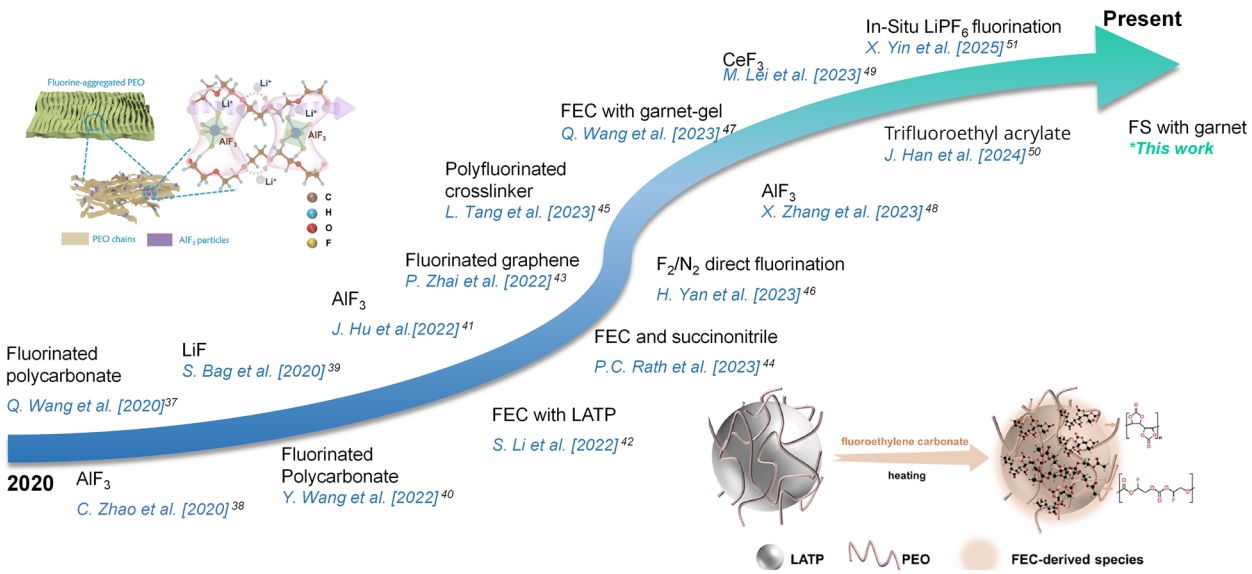

Scheme 1 Recent literature reports on various interfacial engineering using fluorine-based modifications for solid-state lithium metal batteries. Adapted with permission from [ref. 41] Copyright 2022 Springer Nature and [ref. 42] Copyright 2022 American Chemical Society.

varying the filler concentration (20%, 40%, and 60%), as detailed in ESI Table S1.† The conductivity plots deduced from the electrochemical impedance spectroscopy (EIS) measurements (Fig. S2†) revealed that maximum conductivity was obtained for a filler concentration of 40%. In addition, increasing the filler concentration to 60% and higher resulted in visible cracks and difficulty in obtaining a mechanically robust membrane. Moreover, constant current cycling with time limitations revealed that the overpotential characteristics at 40% ceramic loading were more optimal as compared to the other two filler concentrations.

The poor performance at 20% filler concentration was attributed to the ease of dendrite growth in the PEO-dominated membrane, while that for 60% could have resulted from the crack/gap-forming nature and agglomeration in the PEO matrix. Based on the conductivity results and the robustness of the membrane (Fig. S3†), a composite electrolyte with 40% ceramic loading was chosen for further modifications *via* additive incorporation.

We modified the composite electrolyte using 4-fluorostyrene (FS) as the additive. First, 10 μl g^{-1} (solid mass) of FS was added to a polymeric slurry with 40% Al-LLZO loading (see the Experimental section, ESI,† for details) to obtain the modified composite polymer electrolyte, CPE(40)FS. It is to be noted that the CPE comprises PEO : LiTFSI in a 5 : 1 weight ratio unless mentioned otherwise. Upon incorporating the additive, the membrane retained good flexibility, with no visible colour change in the electrolyte film (Fig. 1a). Fig. 1b shows a cross-sectional scanning electron microscopy (SEM) image of the membrane, which reveals a thickness of 110 μm. A magnified SEM image of the film is displayed in Fig. 1c, which clearly depicts the distribution of the filler particles throughout the bulk of the electrolyte. In addition, the homogenous distribution of the fillers across a larger landscape of the polymer matrix is shown in the SEM image in Fig. 1d.

The XRD patterns of the composite electrolyte with and without FS is compared with that of bulk Al-LLZO in Fig. 1e. As the garnet loading is high, the membranes show sharp peaks that were ascribed to Al-LLZO. We conducted thermogravimetric analysis (TGA) to substantiate the filler loading, and the weight loss recorded from the TG curves revealed that CPE(40) and CPE(40)FS stabilize at approximately 40%, reconfirming the fraction of Al-LLZO in the composite (Fig. 1f). The glass transition temperature, T_g, indicates the temperature where the

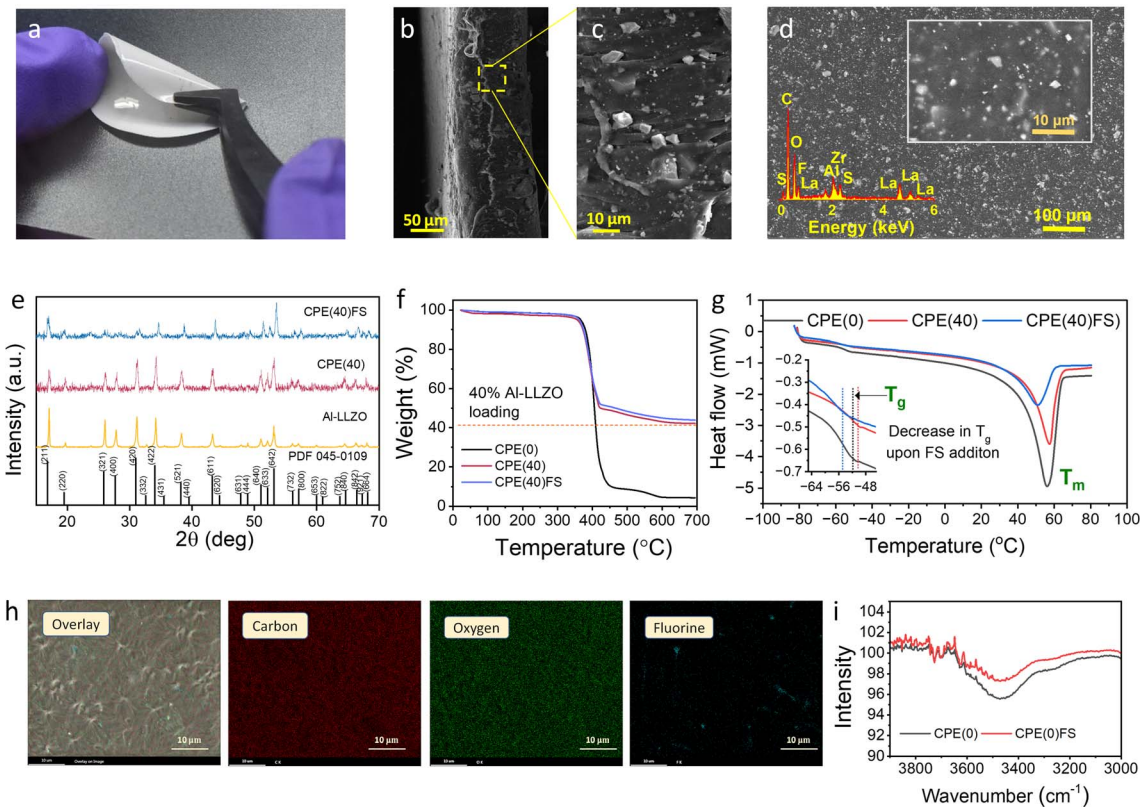

Fig. 1 Physicochemical characterisation of the composite polymer electrolyte. (a) Digital photograph showing the physical appearance of the CPE(40)FS flexible composite membrane. (b) Cross-sectional SEM image of the membrane, revealing a thickness of approximately 110 μm. (c) Enlarged view of the fractured region, and (d) a top-down view in the SEM image of the membrane depicting the distribution of ceramic particles in the membrane (inset: magnified view of the SEM image and the SEM-EDX spectra of the sample). (e) X-Ray diffraction patterns of the Al-LLZO filler, CPE (40), and CPE(40)FS. Comparison of (f) TG curves and (g) DSC curves (swept from −80 °C to 80 °C at a scan rate of 10 °C min^{-1}) of the composite membranes. (h) SEM-EDS elemental mapping of a CPE(40)FS membrane to trace the distribution of fluorine. (i) Representative FT-IR spectra of CPE(0) and CPE(0)FS.

onset of polymeric motions in the amorphous phase is observed, causing a transition from the crystalline to the elastic state.

Plasticisers such as succinonitrile and ionic liquids have been used to alter the T_g of the PEO matrix and enhance the conductivity.[55,56] The T_g values of CPE(40)FS and CPE(40) with Al-LLZO-LiTFSI–PEO are −53.8 °C and −49.9 °C, respectively, as seen from Fig. 1g. The lower T_g for the composite electrolyte upon incorporating FS indicates that the FS also introduces a strong plasticising effect and further reduces the crystallinity of the LiTFSI–PEO matrix, which is beneficial for enhancing the conductivity of composite electrolytes. With the addition of FS, the melting point of the polymer (T_m) decreased from 56 °C to 51 °C because of the potential fluorination/interaction of PEO segments by FS moieties. On comparing CPE(0) and CPE(40), no noticeable shift was seen in the T_g and T_m values with garnet loading.[57] After additive incorporation, it has been a vital challenge to obtain a homogeneous distribution of fluorine in the polymer matrix.

Owing to the high garnet loading, the membrane also demonstrated appreciable thermal stability up to 120 °C, as seen in ESI Video VS1.†

To validate the same, SEM-energy dispersive X-ray spectroscopy (EDS) elemental mapping was carried out, which revealed the presence of carbon, oxygen, and fluorine elements(Fig. 1h). The mapping revealed a significant distribution of F over the entire scan region. To further understand the nature of bonding, we carried out Fourier transform infrared (FT-IR) spectroscopy studies. The FT-IR spectra of CPE(0) and CPE(0)FS were measured and are depicted in Fig. 1i. To avoid ambiguity with Al-LLZO interference, the membranes were prepared without fillers. A significant decrease in the peak intensity at 3400 cm^{-1} was noted. This peak was ascribed to the characteristic OH vibration of PEO, and the decrease in the peak intensity was attributed to the interaction of FS with PEO.[41]

An important property of the FS-added CPE is the significantly enhanced ionic conductivity[58] (Fig. 2a). The Nyquist plot of both membranes obtained at 55 °C is provided in Fig. 2b. The ionic conductivities of the CPE(40) and CPE(40)FS membranes estimated from the plot were 3.3×10^{-5} and 1.0×10^{-4} S cm^{-1}, respectively. Although the structure–property relationship of ion transport in the composite electrolytes remains unclear, activation energy is an assertive indicator.[59]

The activation energies for CPE(40) and CPE(40)FS estimated from the slope of the Arrhenius plot are 1.23 eV and 0.77 eV, respectively. Also, the transference number estimated from chronoamperometry and EIS measurements (Fig. 2c), following the Bruce–Vincent method, is 0.67, which is appreciable for PEO-based polymeric electrolytes. The PEO and salt pathway might contribute to anion migration (typically giving t_{Li^+} <0.5), and hence, we see a slightly lower transport number compared to typical single ion-conducting electrolytes.

As FS is a new electrolyte additive, testing its stable operation window *vs.* the alkali metal anode is vital for rechargeable metal battery applications. It can be seen from Fig. 2d that the membrane has a safe operation limit of 5 V *vs.* Li/Li^+. Fluorine addition modifies the EO groups, thereby turning them into a more stable host for Li^+cations.[60] Because these membranes exhibit superior oxidative stability under high-voltage conditions resulting from the F-rich domains,[61] they are viable for potential application in full cells with high-voltage cathodes. The inclusion of any additive may cause alteration in the SEI due to the strong oxidising ability of the lithium metal. Hence, it is vital to confirm the compatibility of the modified electrolyte with lithium by monitoring the impedance evolution of the electrolyte sandwiched between lithium electrodes. It is evident from Fig. 2e that the symmetric cell with the FS-added electrolyte membrane traces a very stable and low R_{ct} (approximately 1600 Ω on day 15) compared to the unmodified electrolyte, for which the R_{ct} value was approximately 6000 Ω during the same time interval, as seen from Fig. 2f and g.

As mentioned earlier, there were irregularities in the overpotential *vs.* time curve for the 40% filler composition (Fig. S3†). However, when the CCD curves of CPE(40) and CPE(40)FS were overlaid one over the other, the modified counterparts exhibited improved stability, flatter curve, and reduced overpotential, reflecting the improvements facilitated by the addition of FS (Fig. 2h). We hence put forth that the FS forms a stable fluorine-rich layer on lithium and ceramic fillers, possibly regulating the lithium-ion conduction pathway and subsequent lithium deposition even at high currents up to 0.5 mA cm^{-2}. Upon reversing the current density to the initial value of 0.1 mA cm^{-2}, the cell preserves its overpotential, indicating good reversibility and regulated lithium deposition.

So far, researchers all over the world explored design strategies to develop reversible and stable deposition and stripping of Li metal to achieve long-term cycling. Given that the current tolerance is appreciable, this facile strategy also enabled exceptionally stable cycling for 2000 cycles at 0.1 mA cm^{-2} (Fig. 2i). The plating overpotentials at the 10^{th} and 2000^{th} cycles are 92 mV and 104 mV, respectively (Fig. 2j). The CPE thus combines the merits of high garnet loading along with effective modification of the interface. The EIS of the cells was performed before and after the cycling studies (Fig. S4†) with an equivalent circuit reflecting good interface stability.

To decipher the role of fluorine incorporation, we carried out a series of experiments and validated them with DFT studies. The Al-LLZO collected by washing the polymeric membrane in acetonitrile was subjected to TEM and EDS mapping (Fig. 3). A very thin protective layer is seen on the surface of Al-LLZO (Fig. 3a and b). Furthermore, the surface of a particle was mapped to determine the composition of the coating. As predicted, the surface of the Al-LLZO particle was wrapped in a thin fluorine-rich layer as evidenced by the EDS mapping (Fig. 3c and d).

Having confirmed the nature of the species covering the Al-LLZO filler, we present a schematic in Fig. 3e of the possible modification introduced in the CPE(40)FS membrane. An F-rich layer is formed on the surface of Li and also on the particle surface (given in green colour), thereby providing a solution to the PEO/ceramic interface resistance. For underpinning the mechanisms that govern the ceramic–polymer interface, DFT studies were carried out to examine the interaction of FS with PEO (Fig. 3f–h). For comparison, fluoroethylene carbonate

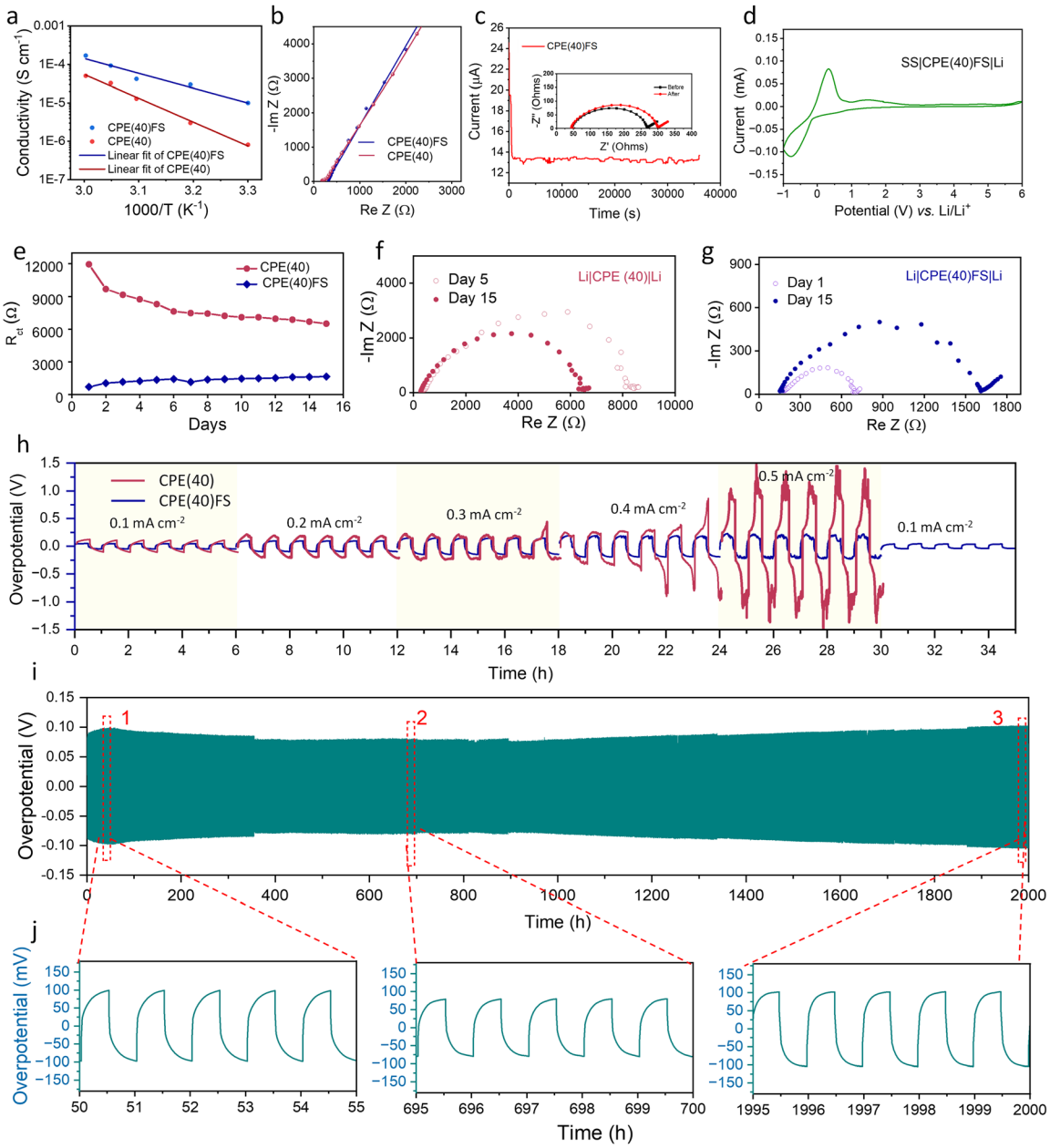

Fig. 2 Characterisation of the ceramic-loaded CPE with and without fluorine incorporation. (a) Arrhenius plots of ionic conductivity as a function of temperature. The solid line is the Arrhenius fit applied to the data. The activation energy is determined from the slope of the fit. (b) Nyquist plot of CPE(40) and CPE(40)FS measured at 55 °C. (c) Transference number (t_{Li}^{+}) estimation using chronoamperometry. (d) CV profile recorded at 0.5 mV s^{-1} to estimate the potential stability window. (e) Interfacial resistance of the Li|Li symmetric cells and the R_{ct} of each CPE. Snippets of a Nyquist plot for the Li|Li symmetric cell comprising (f) CPE(40) and (g) CPE(40)FS. (h) The CCD test curves for CPE(40) (dotted line) and CPE(40)FS in lithium symmetric cells with increasing current densities ranging from 0.1 to 0.5 mA cm^{-2} at a step size of 0.1 mA cm^{-2}. (i) Galvanostatic cycling stability of CPE(40)FS at a current density of 0.1 mA cm^{-2} for 0.5 h in a lithium symmetric cell at 55 °C, and (j) enlarged regions of the cycling profile from three regions of the stability curve.

(FEC), which is the most common F-based additive, was investigated using computations and experiments. The computed binding energy, (ΔG_{BE}) (eqn (S1), ESI†) of Li with PEO (Li-PEO), PEO in the presence of FS (Li-FS-PEO), and PEO in the presence of FEC (Li-FEC-PEO) follows the trend for (ΔG_{BE}) values:

Li-PEO (−4.32 eV) < Li-FEC-PEO (−3.83 eV) < Li-FS-PEO (−3.38 eV).

The more positive Li-ion binding energy upon the introduction of FS/FEC to the PEO polymer matrix suggests that Li-ion-hopping through the PEO chain will be more facile in the presence of these additives. The comparatively more positive (ΔG_{BE}) for PEO-FS as compared to PEO-FEC is also in agreement with the experimentally observed trend in ionic conductivity. Moreover, we noted more positive binding energy for the Li

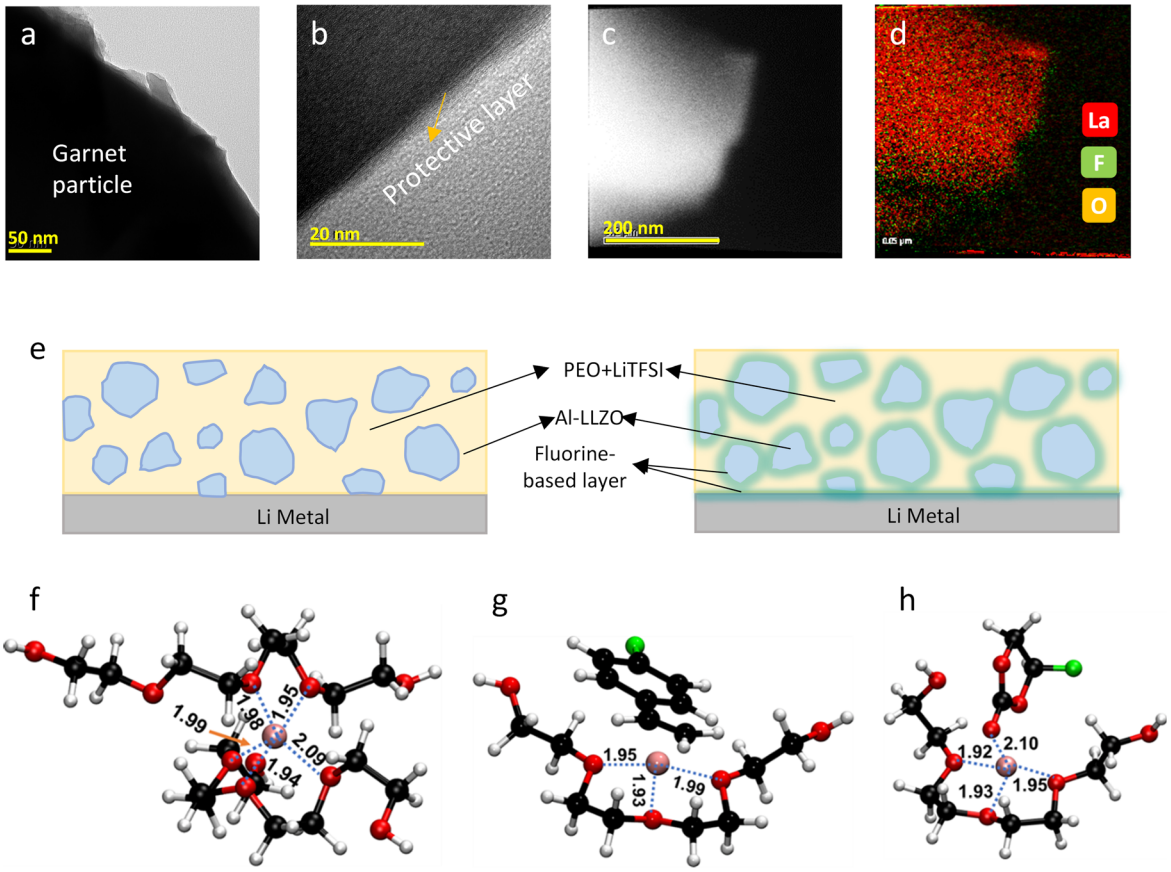

Fig. 3 The surface of Al-LLZO formed by coupling *in situ*-formed lithiophilic fluorine species on the surface. (a) HR-TEM image of the Al-LLZO surface with a height profile of the surface coating. (b) Magnified HR-TEM image showing the fringes at the surface. TEM-EDS mapping of (c) Al-LLZO represented in (d) with F, La, and O, mapped in green, red, and yellow, respectively. (e) Schematic illustration of the possible distribution of Al-LLZO particles in pristine and modified CPEs. Optimised structures of the (f) Li-PEO, (g) Li-FS-PEO, and (h) Li-FEC-PEO complexes with crucial distances (in Å) labelled. Atom color codes: C (black), O (red), H (white), F (green), and Li (pink).

complexes of FS and FEC molecules (−1.11 eV and −1.64 eV, respectively) as compared to the Li complexes of a single PEO chain (−3.03 eV) (Table S2†). The introduction of the additives between the polymer chains thus weakens the interchain interactions, which is evident from the decrease in free hydrogen bonds of PEO as substantiated earlier[41] by FT-IR studies (Fig. 1i), and could result in improved Li-ion-hopping kinetics.

To further evaluate the potential and feasibility of CPE(40)FS for practical applications, full-cell studies were conducted. A Li anode was paired with a $LiFePO_4$(LFP) cathode to assemble an all-solid-state lithium metal battery (ASLMB), as schematically depicted in Fig. 4a. Electrochemical studies to understand the kinetics of charge transport and evaluation of the cycling performance are discussed below. Fig. 4b shows the cyclic voltammograms of the ASLMB with CPE(40)FS electrolyte recorded at different scan rates ranging from 0.2 to 1 mV s^{-1}. The profile shows distinct peaks congruent to the Li//LFP redox couple at their respective potentials. As enhancement in the ionic conductivity should be reflected in the diffusion kinetics of the lithium-ion, we attempted to highlight the improvement by estimating the *b*-values from CV using the relation $i = \nu^b$.[62]

The relationship reliably allows one to capture the *b*-value, which determines two well-defined conditions: for $b = 0.5$, the current is controlled by semi-infinite linear diffusion, which could indicate a faradaic intercalation process, and $b = 1$ is attributed to a surface-controlled capacitive response.[63] From Fig. 4c, the *b*-value was estimated to be approximately 0.69 and 0.58 in the anodic and cathodic regions, respectively, indicating a more diffusion-limited reaction process.[64,65] The galvanostatic intermittent titration technique (GITT) was used to estimate the diffusion coefficient of Li ions in the LFP cathode. A GITT intermittent cycling curve and the corresponding regions of the profile used for the calculation of the diffusion coefficient are presented in Fig. 4d and e, respectively. The *D*-value was calculated using eqn (S5), as detailed in the ESI.†

Although we predicted a low *D*-value because of the PEO-based solid-state configuration, here, the *D*-value was estimated to range in the order of 10^{-12} to 10^{-13} cm^2 s^{-1} during charging and discharging (Fig. 4f and g), which is well in accordance with recent reports.[66] Concomitant to the *b*-values obtained through CV, the GITT results also show that the addition of FS to the composite electrolyte (CPE(40)FS) improved the overall cell performance. This can be attributed to

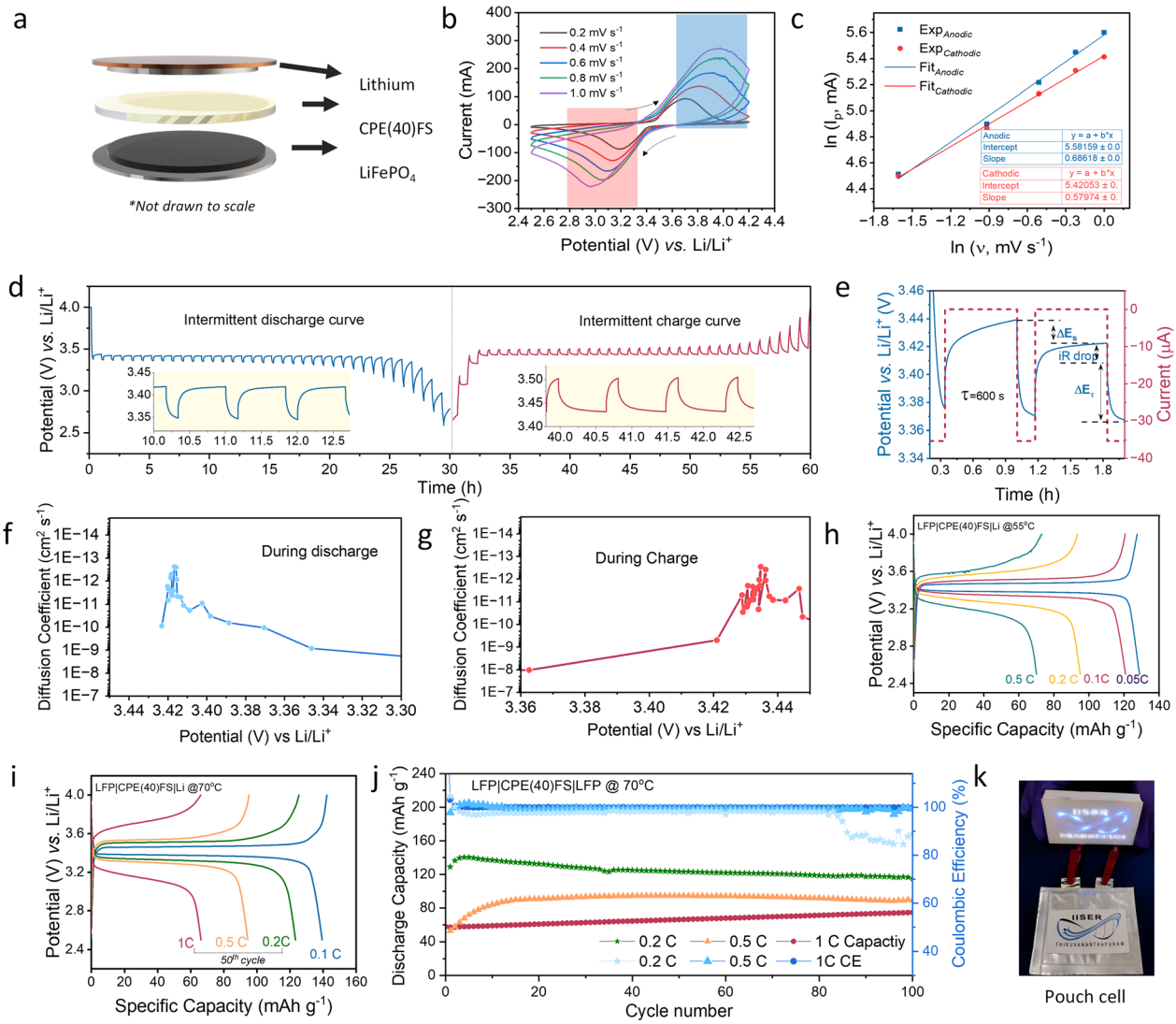

Fig. 4 Electrochemical performance of all-solid-state Li//LFP cells. (a) Schematic of a full cell fabricated for the electrochemical studies where the individual components are labelled alongside. (b) Cyclic voltammograms recorded at various scan rates. (c) ln *v vs.* ln I_p plot to deduce the *b*-value from the slope of the fitted anodic and cathodic regions. (d) GITT curves of the full cell during discharge and charge obtained with a current flux of 35 μA for 40 min, followed by relaxation for 10 min. (e) Magnified GITT curve marking the parameters required for the estimation of the diffusion coefficient. Variation of diffusion coefficient values as a function of cell potential during (f) discharge and (g) charge. Galvanostatic charge–discharge studies of a Li//LFP full cell with the CPE(40)FS membrane as the electrolyte at (h) 55 °C and (i) 70 °C. (j) Long cycling studies of the full cell cycled at different current rates performed at 70 °C. (k) Digital photograph of the fabricated all-solid-state full cell in pouch format with proof-of-concept demonstration.

the ion-conducting inorganic coating on the lithium anode and the surface of garnet particles with LiF-containing species, whose bulk and interfacial ionic conductivities span the range 10^{-6}–10^{-2} S cm^{-1} at ambient temperature.[67]

To gather additional data, galvanostatic cycling studies were carried out at 55 °C for coin-type full cells, and the results are presented in Fig. 4h. Unlike conventional polymer electrolytes, a relatively flat cycling profile was obtained with a polarization gap less than 200 mV at 0.1C (Fig. 4h). The cell delivered a discharge capacity of 126, 122, 97, and 73 mA h g^{-1} at 0.05, 0.1, 0.2, and 0.5C, respectively, with appreciable reversibility of 138 mA h g^{-1} when cycled back at 0.05C at 55 °C (Fig. 4h, S5a and b†).

A post-cycling cross-sectional SEM image (Fig. S5c†) of the cell shows the thickness of individual components, and there was good adhesion between the electrode and electrolyte without any void formation. As a reflection of cycling stability, long cycling of the full cell was carried out. Analogous to our previous findings, the cells exhibited superior cycling stability when cycled at 0.5C for 500 cycles at 55 °C (Fig. S5d†). The FS addition not only introduced a stable anode electrolyte interface, but also facilitated a stable cathode electrolyte interface (CEI), eliminating the need for additional interface modifications.[68,69]

Although the cell delivered a stable capacity for 500 cycles at the 0.5C-rate during long cycling, we noted that increased

capacity was attainable. We attempted to cycle the cell at a slightly elevated temperature of 70 °C, resulting in an improved CEI with a higher discharge capacity of 140 mA h g^{-1} at the 0.1C-rate (Fig. 4i). Similarly, long cycling studies at different rates shown in Fig. 4j further reflect the enhanced cathode interface, which facilitated easier access to the active material and, in turn, offered a higher discharge capacity. The introduction of the FS additive presumably reduced the energy barrier for Li-ion transport and enabled good rate performance.[70] A demonstration of the flexibility of a pouch cell shown to light a light-emitting diode (LED) device (Fig. 4k) is presented in ESI Video VS2.†

To further confirm and ascribe the origin of the F-rich layer to FS additive, we carried out a number of control experiments following in-depth XPS analyses (Fig. S6–S10†). The spectra were corrected to C–C/C–H bonds at 284.5 eV throughout the study. As a benchmark, the XPS plots of PEO and FS are presented in Fig. S6.† For FS, the C 1s and F 1s peaks at 289.3 eV and 686.2 eV were ascribed to C–F bonds of the FS molecule, respectively. For the PEO–FS composite, a significant redshift was seen for the C–F bond in F 1s that was possibly attributed to the interaction of PEO with the FS molecule, in accordance with the DFT studies.[71] Moving to the XPS analysis of the electrolyte membrane, three samples, namely, CPE(40), CPE(40)FS, and CPE(40)FS membrane post-cycling, were initially studied, and the deconvoluted spectra are labelled with the representative species (Fig. S7†).

It is worth mentioning that, although the XPS plots for CPE(40) and CPE(40)FS are similar, the intensity of the peak ascribed to Li–F is more significant in the FS-added membrane. The same peak is evident in the cycled CPE(40)FS as well. This substantiates our claim that F-rich species are present in the sample. However, to further support our claim that the Al-LLZO fillers are wrapped with an F-rich interface, Al-LLZO particles were washed, recovered from the composite electrolyte, and analysed. To achieve this, a piece of CPE(40)FS was dissolved in acetonitrile to wash off the salt and polymer matrix. After three washes (with the last wash in *iso*-propanol), the sample was subjected to mild centrifugation to collect the Al-LLZO. The XPS spectra of the thus-obtained sample are presented in Fig. S8.†

As validation, Li–F peaks were found in the F 1s and Li 1s spectra.[72] Again, there might be a possibility that the Li–F is a repercussion due to LiTFSI. Hence, another reference composite electrolyte was prepared as a test membrane by replacing LiTFSI with $LiClO_4$. The membrane is denoted as CPE'(40)FS. The F 1s spectra of the pristine CPE'(40)FS show only one peak attributed to C–F (Fig. S9†). To substantiate our claim, the emergence of a Li–F peak was evident for the $LiClO_4$ membrane after cycling. Similar observations were also seen in the Li 1s spectrum.

As FEC is one of the commonly studied F-based additives, the same set of experiments was performed and FS was replaced with FEC, and LiTFSI with $LiClO_4$. The composite membrane thus prepared was coined CPE'(40)FEC. The deconvoluted XPS spectra of CPE'(40)FEC before and after cycling are shown in Fig. S10.† Not only was the Li–F signal weak, but an additional peak at 689 eV, attributed to decomposed FEC–PEO products, was seen. Nevertheless, a very weak signal of Li–F was present on the surface of the washed Al-LLZO, unlike the FS counterpart, thereby establishing that FS is a more optimal additive than FEC.

Finally, to compare the performance of the CPE(40)FS electrolyte with the commonly used FEC, a composite electrolyte with the same ratio of FEC was prepared instead of FS under the same experimental conditions, and the performance was evaluated. The membrane, CPE(40)FEC, exhibited lower ionic conductivity compared to the FS counterpart (Fig. S11†), and an activation energy of 1.1 eV was obtained, which lies between that of CPE(40) and CPE(40)FS. Furthermore, the improved ionic conductivity observed in the presence of FS compared to FEC is in accordance with the DFT-based binding energy calculations (Fig. 3f–h). Also, a change in colour to pale yellow was noted for the CPE(40)FEC membrane (Fig. S12†), which could be attributed to some reaction intermediates.

Hence, we propose that FS is an economical and more efficient replacement for the FEC additive, and it can enhance the kinetics and offer higher compatibility with a metal anode. The cycling performance of our additive-incorporated composite electrolyte was compared with that from recent reports and is consolidated and presented in Tables S3 and S4.†

In the case of solid-state batteries with ceramic solid electrolytes, the abrupt change in electrical potential, the interface instability, and contact issues between the cathode and electrolyte remain significant challenges. Many strategies, such as co-sintering, interface softening, and buffer layer incorporation, have been implemented as solutions to these challenges.[73–75]

We further explored the potential application of our optimized composite electrolyte as an interface modifier in the studied Li//LFP full cells.[76–78] A proof-of-concept study of CPE(40)FS as an interface layer for the cathode side was performed by fabricating an all-solid-state battery with the Al-LLZO pellet (Fig. 5a). On the anode side, graphite was coated on Al-LLZO to improve the ion conduction and prevent dendrite

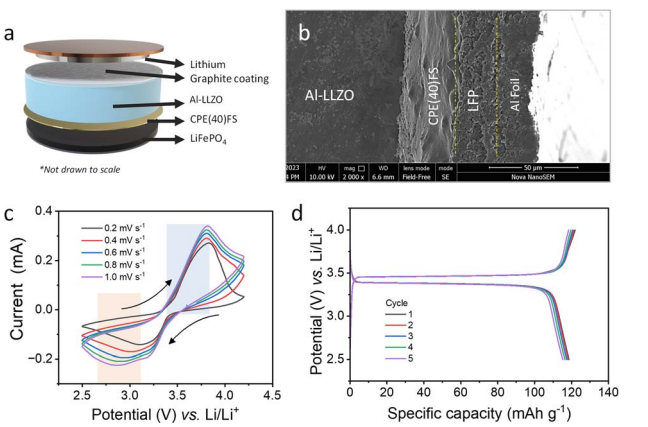

Fig. 5 (a) Schematic representation of the individual layers of the full cell comprising CPE(40)FS as a cathode interface modifier. (b) Cross-sectional SEM image of the cathode side of the full cell showing the individual layers of the cathode, polymeric interface, and the dense Al-LLZO pellet. (c) CVs recorded at different scan rates, and (d) galvanostatic cycling profiles of the full cell tested at a 0.1C-rate at 70 °C.

growth across the Li and Al-LLZO interface.[79] The CPE(40)FS membrane was used as an interface layer at the cathode side with the LFP cathode.

Unlike many reports showing full-cell cycling studies of all-solid-state batteries by wetting the cathode side with a few drops of liquid electrolyte, our full cells are fabricated without liquid electrolyte wetting. The cross-sectional SEM image in Fig. 5b explicitly shows the polymer layer between the cathode and Al-LLZO with well-defined boundaries. The electrochemical studies were carried out at an elevated temperature of 70 °C. The cyclic voltammograms recorded at different scan rates from 0.2 to 1 mV s^{-1} show clear and well-defined redox peaks ascribed to the oxidation/reduction signals from the LFP cathode (Fig. 5c). Furthermore, cycling studies were carried out at a 0.1C-rate, and the cell delivered an initial capacity of 120 mA h g^{-1} with minimum polarization (Fig. 5d).

Post-mortem cross-sectional SEM imaging was carried out on the cycled cells, and is presented in Fig. S13.† The polymer acts as a cushioning layer between the LFP cathode and the Al-LLZO electrolyte, thereby improving the ion transport kinetics. The results presented here are preliminary, and we are in the process of optimizing the pellet thickness, preparing composite electrolytes,[80] cathodes,[81] and tuning the stack pressure[82] or temperature to achieve improved rate capability. This work extends to the larger narrative of a universal interface modifier for various alkali metal anodes with different halide-incorporated styrenes as additives.

Conclusions

Herein, we introduced a new strategy to create a fluorine-rich interface for lithium anodes and the ceramic fillers in the composite polymer electrolyte, enabling the development of dendrite-free lithium metal anodes and thus promoting the practical application of flexible all-solid-state lithium batteries. We showed that a CPE prepared with a high ceramic loading of 40%, and incorporating a new fluorine-based additive, namely fluorostyrene, exhibited high Li-ionic conductivity (10^{-4} S cm^{-1} at 55 °C), and good cycling stability when tested in Li|Li symmetric cells and Li//LFP full cells.

The fluorine-rich lithiophilic layer favours rapid Li-ion transport at the interface and was shown to effectively suppress the dendritic growth at the anode/solid electrolyte interface. The FS-incorporated high ceramic-loaded membranes were further studied as cathode interface modifiers in Li//LFP full cells. Theoretical and control experimental studies provided further insights into the mechanism, thus validating the performance enhancement. Future research will envisage the prospects of similar halide-functionalized styrene for alkali metal batteries.

Data availability

The data for the article "Fluorine-rich Interface for Garnet-based High-Performance All-solid-state Lithium Batteries" are available at the Open Science Forum at Shaijumon, M. M. (2025, February 9). Solid-state battery. Retrieved from https://www.osf.io/4wpts/.

Author contributions

SS, IMS, and SG: conceptualization, data curation, formal analysis, investigation methodology, writing – original draft; AVG and SK: conceptualization, data curation, formal analysis, funding acquisition, investigation, validation, writing – original draft; MMS: conceptualization, funding acquisition, project administration, resources, supervision, validation, writing – review and editing.

Conflicts of interest

There are no conflicts to declare.

Acknowledgements

The authors acknowledge IISER Thiruvananthapuram for the financial and infrastructural support. MMS greatly appreciates the financial support from the Department of Science & Technology, Govt. of India [DST/TMD/IC-MAP/2K20/01]. SK thanks IIT Madras for the New Faculty Seed Grant (NFSG), IP22230585NFSC009001. AVG thanks the SRM Institute of Science and Technology, Kattankulathur, for the facilities and support. SK and AVG thank IIT Madras and the Centre for Atomistic Modelling and Materials Design (CAMMD) for the HPC facilities.

Notes and references

1 C. Zhang, X. Zhao, R. Sacchi and F. You, *Nat. Commun.*, 2023, **14**, 1616.
2 A. K. Nayak, B. Ganguli and P. M. Ajayan, *Energy Rep.*, 2023, **9**, 3508–3530.
3 Z. Yang, H. Huang, F. Lin, Z. Yang, F. Lin and H. Huang, *Adv. Energy Mater.*, 2022, **12**, 2200383.
4 M. Armand and J. Tarascon, *Nature*, 2008, **451**, 652–657.
5 V. Surendran and V. Thangadurai, *ACS Energy Lett.*, 2025, **10**, 991–1001.
6 D. Doughty and E. P. Roth, *Electrochem. Soc. Interface*, 2012, **21**, 37–44.
7 Y. Luo, Z. Rao, X. Yang, C. Wang, X. Sun and X. Li, *Energy Environ. Sci.*, 2024, **17**, 7543–7565.
8 C. Y. Wang, T. Liu, X. G. Yang, S. Ge, N. V. Stanley, E. S. Rountree, Y. Leng and B. D. McCarthy, *Nature*, 2022, **611**, 485–490.
9 L. L. Lu, Y. Y. Lu, Z. X. Zhu, J. X. Shao, H. Bin Yao, S. Wang, T. W. Zhang, Y. Ni, X. X. Wang and S. H. Yu, *Sci. Adv.*, 2022, **8**, 6624.
10 B. Liu, Y. Jia, J. Li, S. Yin, C. Yuan, Z. Hu, L. Wang, Y. Li and J. Xu, *J. Mater. Chem. A*, 2018, **6**, 21475–21484.
11 J. Janek and W. G. Zeier, *Nat. Energy*, 2016, **1**, 16141.
12 J. Janek and W. G. Zeier, *Nat. Energy*, 2023, **8**, 230–240.
13 S. Randau, D. A. Weber, O. Kötz, R. Koerver, P. Braun, A. Weber, E. Ivers-Tiffée, T. Adermann, J. Kulisch,

W. G. Zeier, F. H. Richter and J. Janek, *Nat. Energy*, 2020, **5**, 259–270.
14 J. Li, C. Ma, M. Chi, C. Liang and N. J. Dudney, *Adv. Energy Mater.*, 2015, **5**, 1401408.
15 D. Lin, Y. Liu and Y. Cui, *Nat. Nanotechnol.*, 2017, **12**, 194–206.
16 W. Xu, J. Wang, F. Ding, X. Chen, E. Nasybulin, Y. Zhang and J. G. Zhang, *Energy Environ. Sci.*, 2014, **7**, 513–537.
17 B. Karasulu, S. P. Emge, M. F. Groh, C. P. Grey and A. J. Morris, *J. Am. Chem. Soc.*, 2020, **142**, 3132–3148.
18 B. Tang, P. W. Jaschin, X. Li, S. H. Bo and Z. Zhou, *Mater. Today*, 2020, **41**, 200–218.
19 R. Murugan, V. Thangadurai and W. Weppner, *Angew. Chem., Int. Ed.*, 2007, **46**, 7778–7781.
20 M. S. Indu, G. V. Alexander, O. V. Sreejith, S. E. Abraham and R. Murugan, *Mater. Today Energy*, 2021, **21**, 100804.
21 S. Wang, H. Xu, W. Li, A. Dolocan and A. Manthiram, *J. Am. Chem. Soc.*, 2018, **140**, 250–257.
22 B. P. Dubey, A. Sahoo, V. Thangadurai and Y. Sharma, *J. Mater. Chem. A*, 2022, **10**, 12196–12212.
23 K. G. Stakem, F. J. Leslie and G. L. Gregory, *Chem. Sci.*, 2024, **15**, 10281–10307.
24 L. Dai, M. Cai, X. Zhou, W. Liang, Z. Zhao, Z. Xia, F. Huang, J. Jiang, W. Jiang, B. Zhang and Z. Ma, *Chem. Sci.*, 2025, **16**, 2453–2464.
25 M. Z. A. Munshi and B. B. Owens, *Polym. J.*, 1988, **20**, 577–586.
26 E. M. Masoud, A. A. El-Bellihi, W. A. Bayoumy and M. A. Mousa, *J. Alloys Compd.*, 2013, **575**, 223–228.
27 D. Lin, W. Liu, Y. Liu, H. R. Lee, P. C. Hsu, K. Liu and Y. Cui, *Nano Lett.*, 2016, **16**, 459–465.
28 S. Liu, W. Liu, D. Ba, Y. Zhao, Y. Ye, Y. Li, J. Liu, S. Liu, W. Liu, Y. Zhao, Y. Ye, J. Liu, D. Ba and Y. Li, *Adv. Mater.*, 2023, **35**, 2110423.
29 F. Zheng, C. Li, Z. Li, X. Cao, H. Luo, J. Liang, X. Zhao and J. Kong, *Small*, 2023, **19**, 2206355.
30 Z. Li, J. Fu, X. Zhou, S. Gui, L. Wei, H. Yang, H. Li and X. Guo, *Advanced Science*, 2023, **10**, 2201718.
31 L. Chen, Y. Li, S. P. Li, L. Z. Fan, C. W. Nan and J. B. Goodenough, *Nano Energy*, 2018, **46**, 176–184.
32 J. Zheng, M. Tang and Y. Y. Hu, *Angew. Chem., Int. Ed.*, 2016, **55**, 12538–12542.
33 A. Gupta and J. Sakamoto, *Electrochem. Soc. Interface*, 2019, **28**, 63–69.
34 Z. Li, H. M. Huang, J. K. Zhu, J. F. Wu, H. Yang, L. Wei and X. Guo, *ACS Appl. Mater. Interfaces*, 2019, **11**, 784–791.
35 M. R. Bonilla, F. A. García Daza, P. Ranque, F. Aguesse, J. Carrasco and E. Akhmatskaya, *ACS Appl. Mater. Interfaces*, 2021, **13**, 30653–30667.
36 H. Huo, Y. Chen, J. Luo, X. Yang, X. Guo and X. Sun, *Adv. Energy Mater.*, 2019, **9**, 1804004.
37 Q. Wang, X. Liu, Z. Cui, X. Shangguan, H. Zhang, J. Zhang, K. Tang, L. Li, X. Zhou and G. Cui, *Electrochim. Acta*, 2020, **337**, 135843.
38 C.-Z. Zhao, Q. Zhao, X. Liu, J. Zheng, S. Stalin, Q. Zhang and L. A. Archer, *Adv. Mater.*, 2020, **32**, 1905629.
39 S. Bag, C. Zhou, P. J. Kim, V. G. Pol and V. Thangadurai, *Energy Storage Mater.*, 2020, **24**, 198–207.
40 Y. Wang, S. Chen, Z. Li, C. Peng, Y. Li and W. Feng, *Energy Storage Mater.*, 2022, **45**, 474–483.
41 J. Hu, C. Lai, K. Chen, Q. Wu, Y. Gu, C. Wu and C. Li, *Nat. Commun.*, 2022, **13**, 1–17.
42 S. Li, G. Sun, M. He and H. Li, *ACS Appl. Mater. Interfaces*, 2022, **14**, 20962–20971.
43 P. Zhai, Z. Yang, Y. Wei, X. Guo and Y. Gong, *Adv. Energy Mater.*, 2022, **12**, 2200967.
44 P. C. Rath, M. S. Liu, S. T. Lo, R. S. Dhaka, D. Bresser, C. C. Yang, S. W. Lee and J. K. Chang, *ACS Appl. Mater. Interfaces*, 2023, **15**, 15429–15438.
45 L. Tang, B. Chen, Z. Zhang, C. Ma, J. Chen, Y. Huang, F. Zhang, Q. Dong, G. Xue, D. Chen, C. Hu, S. Li, Z. Liu, Y. Shen, Q. Chen and L. Chen, *Nat. Commun.*, 2023, **14**, 1–10.
46 H. Yan, T. Wang, L. Liu, T. Song, C. Li, L. Sun, L. Wu, J. C. Zheng and Y. Dai, *J. Power Sources*, 2023, **557**, 232559.
47 Q. Wang, Y. Su, W. Zhu, Z. Li, D. Zhang, H. Wang, H. Sun, B. Wang, D. Zhou and L. Z. Fan, *Electrochim. Acta*, 2023, **446**, 142063.
48 X. Zhang, M. Zhang, J. Wu, X. Hu, B. Fu, Z. Zhang, B. Luo, K. Khan, Z. Fang, Z. Xu and M. Wu, *Nano Energy*, 2023, **115**, 108700.
49 M. Lei, X. Wu, Y. Liu, K. Chen, J. Hu and C. Li, *Nano Res.*, 2023, **16**, 8469–8477.
50 J. Han, M. J. Lee, J. H. Min, K. H. Kim, K. Lee, S. H. Kwon, J. Park, K. Ryu, H. Seong, H. Kang, E. Lee, S. W. Lee and B. J. Kim, *Adv. Funct. Mater.*, 2024, **34**, 2310801.
51 X. Yin, Y. Guo, S. Chi, Y. Jia, F. Li, J. Qi, X. Yi, S. Wu and Q.-H. Yang, *J. Am. Chem. Soc.*, 2025, **147**, 4393–4402.
52 C. Gong, S. D. Pu, X. Gao, S. Yang, J. Liu, Z. Ning, G. J. Rees, I. Capone, L. Pi, B. Liu, G. O. Hartley, J. Fawdon, J. Luo, M. Pasta, C. R. M. Grovenor, P. G. Bruce and A. W. Robertson, *Adv. Energy Mater.*, 2021, **11**, 2003118.
53 K. Schroder, J. Alvarado, T. A. Yersak, J. Li, N. Dudney, L. J. Webb, Y. S. Meng and K. J. Stevenson, *Chem. Mater.*, 2015, **27**, 5531–5542.
54 G. M. Veith, M. Doucet, R. L. Sacci, B. Vacaliuc, J. K. Baldwin and J. F. Browning, *Sci. Rep.*, 2017, **7**, 1–15.
55 C. Zhu, H. Cheng and Y. Yang, *J. Electrochem. Soc.*, 2008, **155**, A569.
56 X. Zhang, C. Fu, S. Cheng, C. Zhang, L. Zhang, M. Jiang, J. Wang, Y. Ma, P. Zuo, C. Du, Y. Gao, G. Yin and H. Huo, *Energy Storage Mater.*, 2023, **56**, 121–131.
57 S. Xu, Z. Sun, C. Sun, F. Li, K. Chen, Z. Zhang, G. Hou, H. M. Cheng and F. Li, *Adv. Funct. Mater.*, 2020, **30**, 2007172.
58 P. Vadhva, J. Hu, M. J. Johnson, R. Stocker, M. Braglia, D. J. L. Brett and A. J. E. Rettie, *ChemElectroChem*, 2021, **8**, 1930–1947.
59 K. L. Zhang, N. Li, X. Li, J. Huang, H. Chen, S. Jiao and W. L. Song, *Advanced Science*, 2022, **9**, 2200213.
60 S. Usta, M. Çelik and T. Çetinkaya, *J. Power Sources*, 2023, **580**, 233404.
61 X. Wang, C. Zhang, M. Sawczyk, J. Sun, Q. Yuan, F. Chen, T. C. Mendes, P. C. Howlett, C. Fu, Y. Wang, X. Tan,

D. J. Searles, P. Král, C. J. Hawker, A. K. Whittaker and M. Forsyth, *Nat. Mater.*, 2022, **21**, 1057–1065.
62 S. Suriyakumar, A. Varma, V. Surendran, K. Jasuja and M. M. Shaijumon, *Batteries Supercaps*, 2022, **5**, e202100243.
63 S. Suriyakumar, A. Mazumder, P. S. Dilip, M. Hariharan and M. M. Shaijumon, *Batteries Supercaps*, 2023, **6**, e202300111.
64 B. Babu and M. M. Shaijumon, *ChemElectroChem*, 2021, **8**, 2180–2185.
65 B. Babu and M. M. Shaijumon, *Electrochim. Acta*, 2020, **345**, 136208.
66 B. Wei, S. Huang, Y. Song, X. Wang, M. Liu, H. Jin and G. Cao, *J. Mater. Chem. A*, 2023, **11**, 11426–11435.
67 C. Fu, V. Venturi, J. Kim, Z. Ahmad, A. W. Ells, V. Viswanathan and B. A. Helms, *Nat. Mater.*, 2020, **19**, 758–766.
68 B. P. Thapaliya, A. Y. Borisevich, H. M. Meyer, X. G. Sun, C. A. Bridges and S. Dai, *Adv. Mater. Interfaces*, 2022, **9**, 2201600.
69 T. Zhang, W. He, W. Zhang, T. Wang, P. Li, Z. M. Sun and X. Yu, *Chem. Sci.*, 2020, **11**, 8686–8707.
70 A. R. Polu, K. Kim, A. A. Kareem, D. Kim, S. Song, S. V. Savilov and P. K. Singh, *J. Power Sources*, 2025, **625**, 235742.
71 W. Feng, P. Long, Y. Y. Feng and Y. Li, *Advanced Science*, 2016, **3**, 1500413.
72 F. J. Simon, M. Hanauer, F. H. Richter and J. Janek, *ACS Appl. Mater. Interfaces*, 2020, **12**, 11713–11723.
73 B. Zahiri, A. Patra, C. Kiggins, A. X. Bin Yong, E. Ertekin, J. B. Cook and P. V. Braun, *Nat. Mater.*, 2021, **20**, 1392–1400.
74 K. G. Stakem, F. J. Leslie and G. L. Gregory, *Chem. Sci.*, 2024, **15**, 10281–10307.
75 D. Ding, H. Ma, H. Tao, X. Yang and L. Z. Fan, *Chem. Sci.*, 2024, **15**, 3730–3740.
76 K. Nie, Y. Hong, J. Qiu, Q. Li, X. Yu, H. Li and L. Chen, *Front. Chem.*, 2018, **6**, 422093.
77 P. Aswathy, S. Suriyakumar, S. A. Kumar, M. S. Oliyantakath Hassan, V. Vijayan and M. M. Shaijumon, *ACS Appl. Energy Mater.*, 2022, **5**, 12592–12601.
78 C. Ouyang, S. Wu, G. Li, N. Zhang, Q. Chen, R. Zhang, H. Sun, C. Zhang, H. Liu and H. Duan, *Mater. Lett.*, 2025, **380**, 137729.
79 Y. Shao, H. Wang, Z. Gong, D. Wang, B. Zheng, J. Zhu, Y. Lu, Y. S. Hu, X. Guo, H. Li, X. Huang, Y. Yang, C. W. Nan and L. Chen, *ACS Energy Lett.*, 2018, **3**, 1212–1218.
80 S. Suriyakumar, R. M. Manoj, S. K. Jayaprakash, S. A. Kumar, K. P. Sudhakaran, V. Vijayan and M. M. Shaijumon, *RSC Appl. Interfaces*, 2024, **1**, 1436–1442.
81 Z. Zeng, J. Cheng, Y. Li, H. Zhang, D. Li, H. Liu, F. Ji, Q. Sun and L. Ci, *Mater. Today Phys.*, 2023, **32**, 101009.
82 C. Lee, S. Y. Han, J. A. Lewis, P. P. Shetty, D. Yeh, Y. Liu, E. Klein, H. W. Lee and M. T. McDowell, *ACS Energy Lett.*, 2021, **6**, 3261–3269.